



# Monitoring and flaw detection during wire-based directed energy deposition using in-situ acoustic sensing and wavelet graph signal analysis

Benjamin Bevans<sup>a,c</sup>, André Ramalho<sup>b</sup>, Ziyad Smoqi<sup>a</sup>, Aniruddha Gaikwad<sup>a</sup>, Telmo G. Santos<sup>b</sup>, Prahalad Rao<sup>a,c</sup>, J.P. Oliveira<sup>b,d,\*</sup>

<sup>a</sup> Mechanical and Materials Engineering, University of Nebraska-Lincoln, Lincoln, NE, USA

<sup>b</sup> UNIDEMI, Department of Mechanical and Industrial Engineering, NOVA School of Science and Technology, Universidade NOVA de Lisboa, 2829-516 Caparica, Portugal

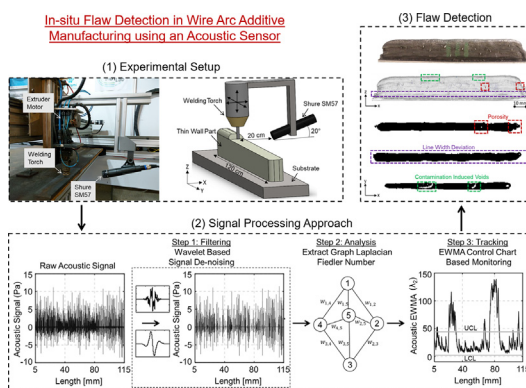
<sup>c</sup> Industrial and Systems Engineering, Virginia Tech, VA, USA

<sup>d</sup> CENIMAT/I3N, Department of Materials Science, NOVA School of Science and Technology, Universidade NOVA de Lisboa, 2829-516 Caparica, Portugal

## HIGHLIGHTS

- The wire-based directed energy deposition process was monitored using an in-situ acoustic sensor installed near the electric arc.
- Onset of flaw formation, such as porosity, variation in line width, and spatter are not readily observable from the raw acoustic sensor data.
- Wavelet integrated graph theory approach is used to analyze the data and extract a single feature, called the Fiedler number.
- Using the Fiedler number to monitor the process, previously undetected flaws were captured with a false alarm rate less than 2%.

## GRAPHICAL ABSTRACT



## ARTICLE INFO

### Article history:

Received 30 August 2022

Revised 28 October 2022

Accepted 7 December 2022

Available online 9 December 2022

### Keywords:

Wire-based directed energy deposition  
Process flaw monitoring  
Acoustic sensor  
Wavelet filtering  
Graph theory

## ABSTRACT

The goal of this work is to detect flaw formation in the wire-based directed energy deposition (W-DED) process using in-situ sensor data. The W-DED studied in this work is analogous to metal inert gas electric arc welding. The adoption of W-DED in industry is limited because the process is susceptible to stochastic and environmental disturbances that cause instabilities in the electric arc, eventually leading to flaw formation, such as porosity and suboptimal geometric integrity. Moreover, due to the large size of W-DED parts, it is difficult to detect flaws post-process using non-destructive techniques, such as X-ray computed tomography. Accordingly, the objective of this work is to detect flaw formation in W-DED parts using data acquired from an acoustic (sound) sensor installed near the electric arc. To realize this objective, we develop and apply a novel wavelet integrated graph theory approach. The approach extracts a single feature called graph Laplacian Fiedler number from the noise-contaminated acoustic sensor data, which is subsequently tracked in a statistical control chart. Using this approach, the onset of various types of flaws are detected with a false alarm rate less-than 2%. This work demonstrates the potential of using advanced data analytics for in-situ monitoring of W-DED.

© 2022 The Authors. Published by Elsevier Ltd. This is an open access article under the CC BY license (<http://creativecommons.org/licenses/by/4.0/>).

\* Corresponding author at: CENIMAT/I3N, Department of Materials Science, School of Science and Technology, NOVA University Lisbon, Caparica, Portugal.

E-mail address: [jp.oliveira@fct.unl.pt](mailto:jp.oliveira@fct.unl.pt) (J.P. Oliveira).

## 1. Introduction

### 1.1. Objectives and Motivation: The need for inline, in-process monitoring during wire-based directed energy deposition (W-DED)

The goal of this work is to detect flaw formation during the wire-based directed energy deposition (W-DED) additive manufacturing process using data acquired from in-situ sensors. Realizing this goal is the first step towards the implementation of closed-loop process control in W-DED, thereby ensuring the functionality and structural integrity of the manufactured parts.

Under the directed energy deposition (DED) family of additive manufacturing processes, material is fed (sprayed or forced) into the focal zone of a high energy source, where it is melted and fused to a previously deposited layer [1]. The material can take the form of powder (P-DED) or wire (W-DED). Likewise, the typical energy sources to melt the material range from laser, electron beam, electric arc, and gas plasma [2]. The specific embodiment of W-DED used in this work (Fig. 1), is the free-form analogue of conventional, and well-known, metal inert/active gas (MIG/MAG) welding. The process is popularly known as wire arc additive manufacturing (WAAM) – an acronym we use in this work to distinguish it from other forms of W-DED [3].

In WAAM an electric arc is maintained between the part and a consumable wire of the material to be deposited. The energy from the electric arc melts the wire feedstock, which is surrounded by a shielding gas (e.g., argon or nitrogen). The shielding gas prevents disruption of the arc, aids in the material transfer, and is also used to protect the molten pool and its surroundings from oxidation. The relative motion of the part and welding torch in three dimensions produces a free-form geometry. Popular materials for the process include non-ferrous metals, such as aluminum and titanium, and ferrous alloys, such as mild steel and stainless steel (this work) [4].

In comparison to powder-based DED (P-DED), WAAM has distinct cost and throughput advantages. For instance, the cost of mild steel welding wire is less than \$10/kg, compared to nearly \$100/kg of metal powder used in P-DED. Similarly, the volumetric deposition rate for WAAM is typically 15 times that of P-DED; the typical volumetric deposition rate of WAAM is  $\sim 50 \text{ mm}^3\text{s}^{-1}$  compared to  $\sim 4 \text{ mm}^3\text{s}^{-1}$  for P-DED [4–5]. Because of these advantages, WAAM has emerged as the additive manufacturing process of choice in low resource settings, and for the fabrication of large volume parts. For example, the WAAM process can be integrated with one or more robots working together to produce parts, such as wind turbines, excavators, and oil drilling equipment, within hours as opposed to weeks it would require with P-DED [6]. The WAAM process also finds unique application for rapid repair and refurbishment, and deposition of heterogeneous materials [7].

Currently, a major bottleneck in wider adoption of the WAAM process is its tendency to create flaws, such as porosity and poor

geometric consistency (distortion) [8]. However, this impediment is prevalent in all fusion-based processes, including P-DED [9]. There are mainly four reasons for flaw formation to occur in WAAM, these are: (i) poor selection of processing parameters, (ii) improper design (geometry) of the part; (iii) sub-standard materials, and (iv) disruption of the arc due to machine faults and stochastic disturbance from the environment, such as interference from contaminants, noting that WAAM is typically used in low resource environments.

To illustrate the foregoing challenges, shown in Fig. 2 is a WAAM part (stainless steel 316L) produced in this work, with accompanying X-ray computed tomography (XCT) slices of this part. Fig. 2(a)–(c) are XCT slices of different layers of the part depicting the presence of flaws. For example, porosity is a primary flaw that is observed in Fig. 2(a). Likewise, in Fig. 2(b) a variation in the width of a track is evident. The voids in Fig. 2(c) are correlated to disruption of the arc due to presence of contaminants, as previously shown by Ramalho et al. [10].

Given the relatively large size and complex geometry of practical WAAM parts, post-process non-destructive testing (NDT) of flaws with XCT is difficult, if not impossible. A typical 250 kV XCT machine can only penetrate through 15 mm of stainless steel material before the occurrence of measurement errors, such as beam hardening [11]. This prevents a thorough non-destructive evaluation of large WAAM components in practice. Hence, in-process monitoring and detection of flaws in WAAM is an urgent and critical requirement.

Considering the foregoing motivation, the objective of this work is to detect flaw formation in WAAM using data acquired from an in-situ acoustic sensor installed in close proximity to the electric arc. To realize this objective, we developed a novel wavelet integrated graph theory approach to filter, process, and monitor the process signatures. The approach has three steps discussed in detail in Sec. 3, these are:

- (1) *Signal Filtering*: The raw data acquired by the acoustic sensors is filtered using wavelet analysis to remove background process noise [12].
- (2) *Signal Processing (Analysis)*: The filtered sensor data is analyzed using a computationally lightweight and tractable spectral graph theory approach [13]. Using graph theory signal analysis, we extract just one feature (signature) called the graph Laplacian Fiedler number ( $\lambda_2$ ) to capture the process dynamics.
- (3) *Signal Monitoring (Tracking)*: The Fiedler number ( $\lambda_2$ ) process signature is tracked in an exponentially weighted moving average (EWMA) control chart. An out-of-control point on the chart indicates an impending process flaw. This quality control chart approach is one of the most intuitive and practitioner-friendly means to monitor and track industrial processes [14].

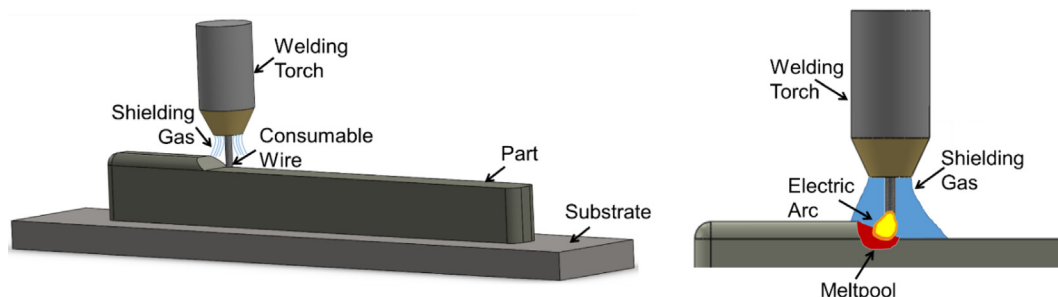
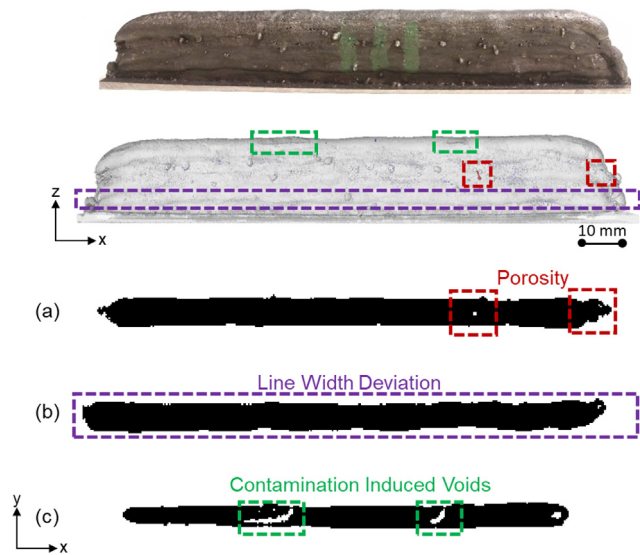


Fig. 1. Schematic of the Wire Arc Additive Manufacturing (WAAM) process. A welding head deposits material via the use of a consumable electrode being melted with an electric arc.



**Fig. 2.** Example of the three major flaws observed in this work: (a) porosity, (b) deviation in geometry of an individual tracks (line width variation), (c) voids due to contamination from the surrounding environment.

The presented approach thus avoids extracting numerous statistical features, and using these features in complex machine learning algorithm for process monitoring. Thus, the approach is amenable for deployment on the shop-floor for real-time monitoring of WAAM. While the approach detects the onset of arc instability, and as a consequence, captures when and where an incipient flaw might occur, a limitation of the approach is that it cannot identify the specific type of flaw formed.

## 1.2. Prior work and novelty

As explained before, the WAAM process has its genesis in fusion welding processes which employ an electrical arc as the heat source. Typically, these processes are monitored and controlled by tracking the electrical current and voltage, wire feed rate, torch travel velocity, and shielding gas flow rate [15]. However such machine-level process monitoring cannot detect faults that occur at the part-level, such as surface contamination, that can ultimately result in flaw formation [3]. Hence, in-situ part-level monitoring is critical for quality assurance in WAAM.

Considering the challenges that WAAM presents to non-destructive testing, several part-level in-process sensor-based monitoring methods have been studied by researchers [16]. A key concern is to devise quantitative, easy-to-implement, and intuitive approaches to detect flaw formation from the large volume of noise contaminated sensor data. Visual sensing, using a CMOS camera, has been applied to determine bead geometry [17], arc length [18], and to determine wire deflection during the deposition process [19]. In a different context, physics-based process modeling has been used for quality assurance in WAAM. For example, Suryakumar *et al.* [20] developed a weld bead model to accurately predict the bead geometry in place of in-situ sensing.

Thermal monitoring has successfully been used to track the temperature between successive depositions using a two-wavelength pyrometer [21], and measure the thermal gradients of parts using an infrared camera [22]. Recently, optical emission spectroscopy (OES) monitoring has been applied to WAAM. For example, Zhang *et al.* [23] used OES to detect porosity in WAAM

parts. Likewise, Hauser *et al.* [24] used OES to detect oxidation of aluminum WAAM parts.

When applied to laser-based additive manufacturing processes, acoustic monitoring has been demonstrated successfully for flaw detection via the use of acoustic emissions (AE) sensors. These AE sensors measure the acoustic waveforms inside a solid material, as opposed to acoustic sensors which measure the acoustic signal in air. Analysis of AE has been used for the detection of porosity and micro-cracks in laser powder bed fusion (LPBF) [25]. Deep learning algorithms have also been applied to AE data to characterize part quality in LPBF [26] and for identification of process instabilities such as balling [27]. In the WAAM process, Zhu *et al.* [28] used an AE sensor with electrical current data to identify a correlation between the droplet transfer mode and power fluctuations.

An emerging method for WAAM monitoring is through the evaluation of the acoustic signatures. Pringle *et al.* [29] proposed a multi-sensor monitoring system that includes an acoustic sensor and presented measurable changes in the acoustic signal resulting from changes in the wire feed and torch speed parameters. While several papers have been published regarding acoustic monitoring in conventional welding processes, their application to WAAM is relatively sparse.

In the context of acoustic sensing in WAAM, Polajnar *et al.* [30] showed that the quality of the weld transfer mode and electric arc have a direct effect on the acoustic signatures during GMAW. Horvat *et al.* [31] identified the mechanisms that generate acoustic signature of the electric arc in GMAW and correlated these to the electric current. Tang *et al.* [32] used acoustic monitoring to identify the arc length in GTAW. Acoustic monitoring has been used successfully for detecting major flaws in single bead depositions [33], and identifying the penetration depth of the molten pool [34]. Representative work towards flaw detection in the WAAM process and their limitations are further summarized in Table 1. These other flaw detection works for the WAAM process have not quantified their false positive and false negative rates, and are simple visual correlations for detecting a WAAM phenomenon (arc length, wire deflection, etc.). These prior works, also do not correlate the signal to flaw formation or part quality, and most are limited to single layer parts only.

Recently, Ramalho *et al.* [10] showed that the effect of surface contaminations in WAAM can be identified based on the acoustic signatures produced, however no other flaw detection was investigated. The acoustic monitoring method proposed in this paper leverages a novel wavelet filtering approach integrated with spectral graph theory to analyze the acoustic data emitted during WAAM. Thus avoiding the use of numerous statistical features and complex machine learning for flaw detection. Instead, the proposed process monitoring approach is based on extracting one statistic (Fiedler number) from the sensor data and tracking this number in a simple and practically intuitive control chart. Consequently, this approach can be applied to the shop floor with minimal changes.

The rest of the paper is organized as follows, the experimental methodology, including the experimental setup is described in Sec. 2. The wavelet-based graph theory approach is described in Sec. 3. The results from applying the approach to the WAAM process is demonstrated in Sec. 4. Conclusions and avenues for future work are summarized in Sec. 5.

## 2. Experimental methodology

### 2.1. Experimental setup

In this work, thin wall parts (AISI 316L stainless steel) were produced with a feedstock welding wire diameter 1 mm. The samples

**Table 1**  
Prior work concerning sensor monitoring in Wire Arc Additive Manufacturing.

Sensors Used	Ref.	Outcome	Limitations
Current & Voltage	[35]	Used machine learning to predict when arc is starting, stopping, nominal, or changing direction	No flaw detected. Only for a single layer
	[36]	Detected large line width changes	No porosity detection
Acoustic Sensor	[37]	Connects major line width changes to a change in the acoustic signal	No prediction, only correlation to single track quality
	[33]	Uses the kurtosis of the acoustic signal to detect large flaws	Single track only
Acoustic Emission	[38]	Measured arc length in GTA-WAAM	No error detection
	[39]	Used AE signals from the substrate to detect quality of metal transfer	Errors not quantified
Laser & CCD Camera	[40]	Measured the surface roughness	Single layer only
CCD Camera	[19]	Used camera to detect deflection of electrode wire	No error detection
	[17]	Used camera to measure and control line width in-situ	Single layer only
	[18]	Measured length of arc to determine if it is strong or weak	No error detection
Spectrometer, Camera, and Structural Acoustic Sensor	[41]	Detects different signal frequency depending on material deposition	No error detection
Laser-Optical-Ultrasonic-Dual (LOUD)	[42]	Measure residual stress, large flaws, and composition	Post process, offline-sensing

are  $\sim 120$  mm long and consist of 11 layers ( $\sim 14.5$  mm height  $\times$  4 mm thick). The processing conditions are reported in Table 2. The WAAM setup, shown in Fig. 3, consists of a metal inert gas welding torch (MIG, Kempi Pro MIG 3200) using Argon gas, with a control unit (Kempi Pro MIG 501) integrated into a custom-built CNC unit.

A Shure SM57 dynamic cardioid microphone, with a frequency response of 40 to 15000 Hz, is attached to the welding torch and translates along with the torch. Hence the microphone is at a constant distance of 200 mm from the arc at all times. The angle of the microphone relative to the substrate is set at  $20^\circ$ , and a data collection rate of 25.6 kHz. Data collection rate of 25.6 kHz was chosen as it was the maximum frequency allowed by the microphone. This combination of distance, angle, and frequency mitigates signal loss resulting from sensor polarity, positioning and the frequency response rate (40 Hz – 15 kHz). Non-destructive part characterization is performed using X-ray computed tomography (XCT) on all samples using a Nikon XTH 255 ST system at a voxel resolution of  $17 \mu\text{m}$ . This was the highest resolution possible given the size and density of the sample. The data collected from the XCT is extracted using the native Volume Graphics software.

**Table 2**  
Process parameters settings used in the experiments.

Sample	Contamination Type	Travel speed	Voltage	Feed Rate	Layer Height	Standoff	Wire Diameter
1	Chalk	300 mm/min	20 V	4 m/min	1.3 mm	8 mm	1 mm
2	Oil	Bi-directional					
3	Sand						

Three distinct thin walls are studied in this work. Each thin wall is deposited with a specific type of contaminant to promote arc instabilities. To explain further, practical WAAM operations are typically conducted without an enclosure, unlike in P-DED or LPBF. As a result, contaminants are liable to infiltrate into the material and disrupt the electric arc, thus causing arc instability. Our previous work, detailed in [10], demonstrated the ability to suppress background noise from the system, such as flow of process gasses, motor, and machine elements through a rigorous cause-effect analysis. As a consequence of this previous work, critical welding process phenomena can be isolated, and used to detect the onset of flaws.

In this work, contaminants are added to cause arc instabilities in a controlled manner at specific locations. We introduce the presence of three types of contaminants (chalk, oil, and sand) that are common in a shop floor environment to simulate disruption of the arc and create flaws in a controlled manner. A type of contaminant is placed at 40 mm intervals on layers 7 and 11 of a thin wall part as shown in Fig. 4. The contaminant used for Sample 1 is chalk; Sample 2 used oil; and Sample 3 used sand. Contaminants are introduced in their respective locations by drilling a flat-bottom hole of  $\phi 2.5 \text{ mm} \times 1 \text{ mm}$ . There is a  $\pm 3 \text{ mm}$  location error along the length in placement of the contaminant due to the manual nature of the operation.

During the manual process of placing these contaminants the time between layers (TBL) was slightly increased. The nominal TBL for all layers, on all samples, was 2 min to allow for ample time to cool the part and reduce the amount of residual stresses in the sample. However, on layer 7 and 11 when the contaminants are placed, the manual operation of placing the contaminants increased the TBL to approximately 4–5 min. The original 2 min TBL is sufficient to cool the sample to a near steady-state temperature well below the material recrystallization temperature, therefore, the additional 2–3 min added to the TBL for layer 7 and 11 would have a negligible effect on the microstructure. Moreover, this work is focused on arc instability, and its consequent effect on flaw formation, as opposed to thermal history. In our future work, we will endeavor to answer the effect of thermal history on flaw formation.

## 2.2. Representative acoustic sensor data

The nature of arc instability generated via chalk contamination in Sample 1 is shown in Fig. 5(a1). Due to its relatively low packing density ( $910\text{--}960 \text{ kg}\cdot\text{m}^{-3}$  [43]), it is hypothesized that the chalk powder is forced out of the cavity by the argon shielding gas ( $0.7 \text{ m}^3\cdot\text{hour}^{-1}$ ). The chalk disturbs the shielding gas and destabilizes the arc. Consequently, the arc is nearly extinguished causing intermittent deposition, resulting in significant line width variations as observed in Fig. 5(a3). Due to the disruption of the argon shielding gas, the chalk contaminations are distinctly discernable in the raw signal (S) in Fig. 5(a2). Apart from the line width variations noted in the XCT slice of the layer shown in Fig. 5(a3), there is a pore at the end of the layer that is not readily discerned in the raw acoustic signal.

Sample 2, Fig. 5(b), which has oil contamination introduced, shows the most severe porosity and spatter formations due to



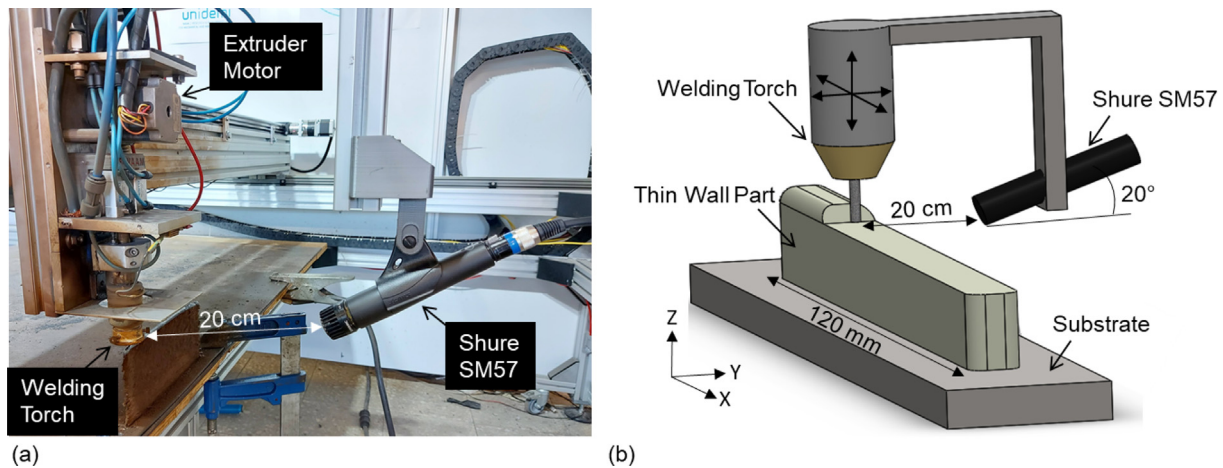


**Fig. 3.** Picture and schematic of the experimental set-up. A Shure SM57 acoustic sensor is attached to the welding torch maintaining a constant distance to the electric arc.

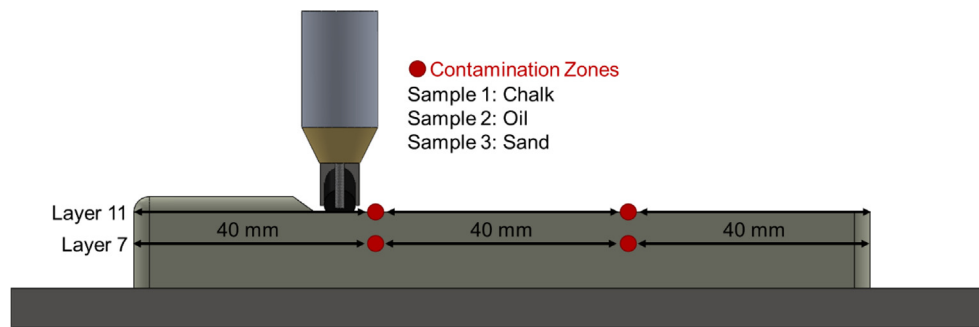


**Fig. 4.** Schematic diagram of the four contamination zone locations used in this work. Contamination is introduced on layer 7 and layer 11 at two locations 40 mm apart.

the low boiling point of oil ( $\sim 300^\circ\text{C}$ ) [44]. As illustrated in Fig. 5 (b1) the oil evaporates instantly due to the moltpool temperature of AISI 316L stainless steel ( $>1450^\circ\text{C}$ ) greatly exceeding the boiling point of oil. Apart from disturbing the shielding gas, this instantaneous boiling of the oil generates large pores and spatter observed on the side of Sample 2, Fig. 5(b3), but not in the other samples. The raw acoustic signal (S) for layer 11 of Sample 2 is depicted in Fig. 5(b2). Despite the large pores observed in Sample 2, the causal arc instability is not readily discerned in the raw signal due to background process noise. Hence, more evolved analysis of the acoustic signal, including the pragmatic filtering of background noise, is required to detect arc instability and flaw formation.

Sand contamination in Sample 3, Fig. 5(c), did not generate readily observable arc instabilities in the acoustic signal Fig. 5 (c2). This is due to a higher packing density of sand in comparison to chalk, in excess of  $1,300\text{ kg}\cdot\text{m}^{-3}$  [45]. Due to its higher packing density, less amount of sand is blown away by the shielding gas compared to chalk. Hence, unlike chalk and oil contaminations, the shielding gas is not disturbed, and the arc is not destabilized. Since the cavity where sand is introduced is only 1 mm in diameter, the electric arc can transition (jump over) the cavity without disrupting the deposition of material as depicted Fig. 5(c1). Therefore, no pore is generated, however, sand is left inside the part. Accordingly, the corresponding acoustic signal (S), in Fig. 5(c2), is devoid of visually prominent disruptions, and the XCT slice depicted in Fig. 5(c3) has minimal flaws in comparison to Samples 1 and 2.

A major insight from this work is that flaws generated by an arc instability on a previous layer have the potential to propagate and generate a flaw on the current layer. This feedback effect is visual-

ized in Fig. 6. This results in some arc instabilities occurring one layer above a flaw created in a previous layer. For example, if a preceding layer has significant porosity, a gap (void) will be encountered by the electric arc when it is directly above the pore in the previous layer. Consequently, the arc can potentially be disturbed causing variation in line width or porosity. In other words, an arc instability initiated in one layer can create flaws in multiple ascending layers.

Apart from material contamination, such arc instabilities can be generated due to inconsistent power supply, flaws in previously deposited layers, disruption of the shielding gas, motion errors, among others. The foregoing arc instability-flaw generation feedback effect results in multifarious flaws, such as porosity, irregular deposition, and spatter that propagate across multiple layers.

### 3. Signal processing using wavelet analysis & graph theory

The signal analysis procedure used in this work consists of three steps schematically detailed in Fig. 7. First, the acoustic signals are filtered using wavelet analysis to remove extraneous background noise and cyclical patterns from the machine. Second, the wavelet filtered sensor data are analyzed using a spectral graph theory approach to extract a single process signature (Laplacian Fiedler number) symptomatic of arc instability. Third, the process signature (Fiedler number) from graph theory is tracked using an Exponentially Weighted Moving Average (EWMA) control chart to determine the occurrence of arc instabilities within a given deposited layer. A limitation with this approach, common to all control chart-based methods, is that it is focused on detecting arc instabil-

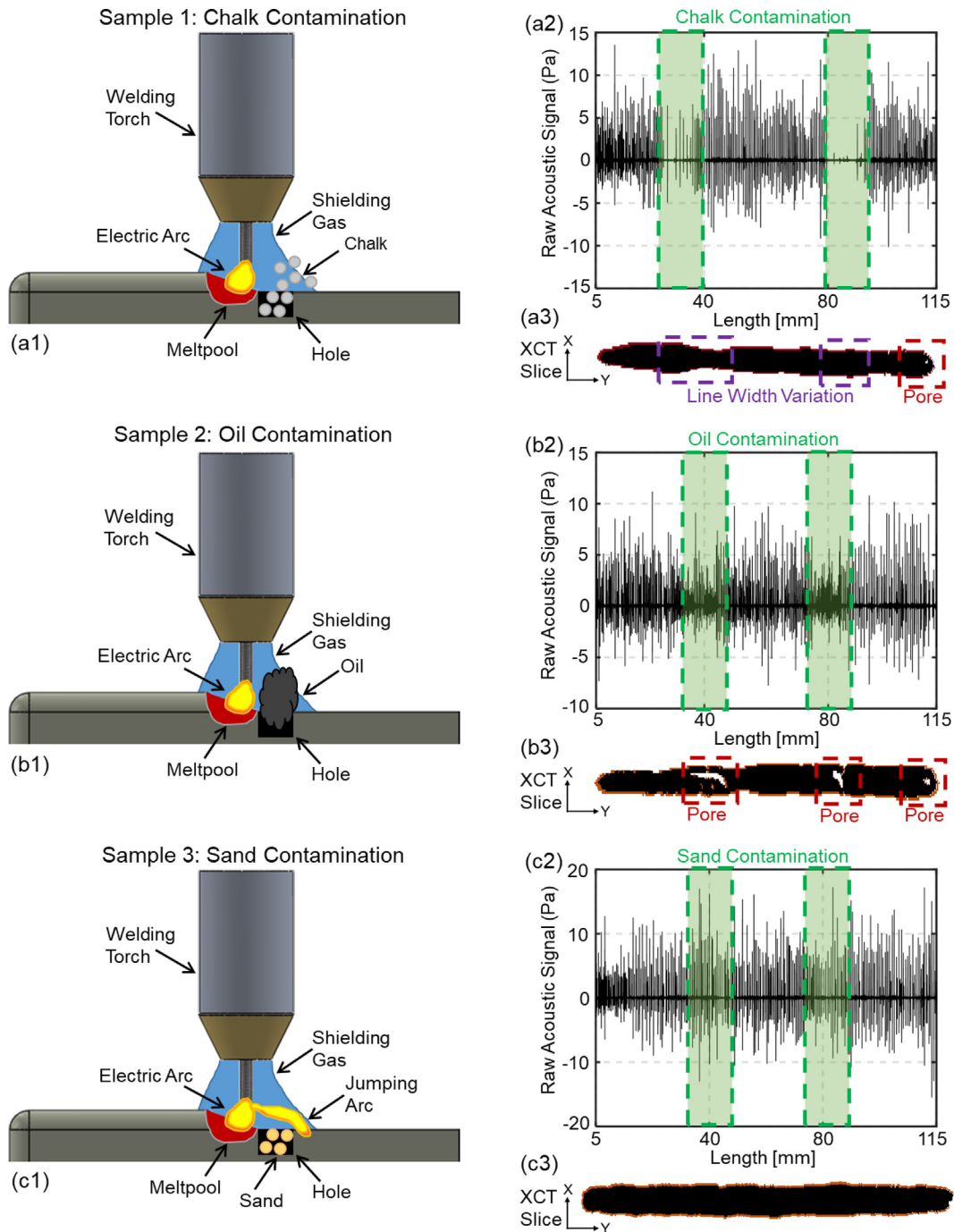


**Fig. 5.** Schematic representation of the effect of the three types of contaminations and the flaws that they generate. (a) details the effect of chalk contamination, (b) shows the effect of the oil contamination, (c) highlights the effect of the sand contamination. Contamination zones are marked in green.

ities (special causes) that are at the root cause for flaw formation, as opposed to capturing specific types of flaws.

### 3.1. Step 1 – Wavelet filtering

A wavelet transform is used to remove the background noise from the machine [12]. Unlike the Fourier transform where the signal is translated and analyzed in the frequency domain, the wavelet transform allows the data to be analyzed in both the frequency and time domains simultaneously, which enables the precise location of a flaw to be detected in-situ.

Another difference between the Fourier and wavelet transforms is the type of basis used to convolve the signal into the frequency domain. In the Fourier transform, the data is convoluted with a sinusoidal basis. In the wavelet transform a large variety of signal basis can be chosen and new (custom) basis can be designed to fit the application. These basis for transforming the signal are called wavelets. There are two distinct advantages of the wavelet transform over Fourier analysis that motivates their use in this work [46]:

- a. Wavelet transforms accommodate non-stationary data where sudden changes can occur, such as arc instability.

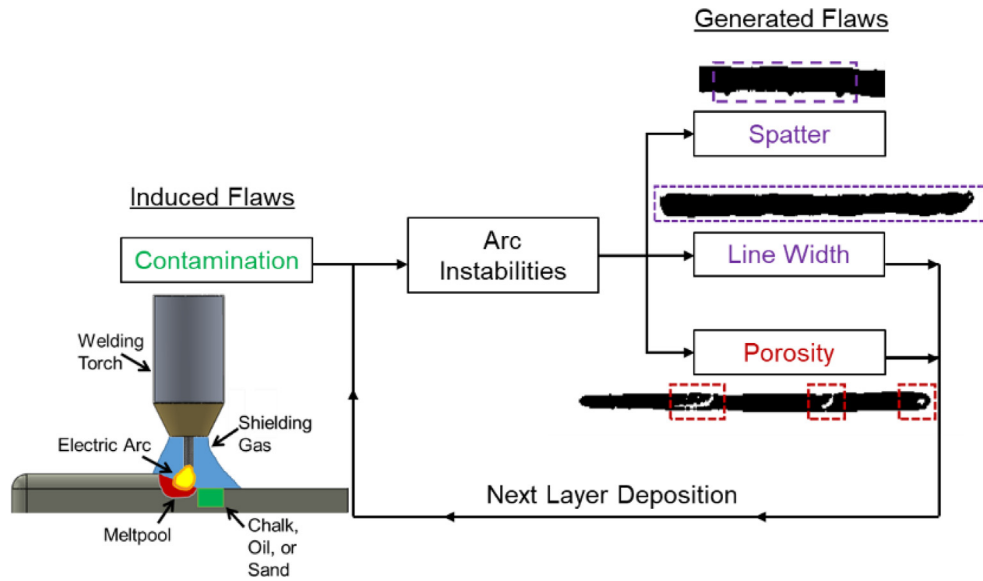


**Fig. 6.** The feedback effect of flaw formation in WAAM. Flaws caused on a previous layer can potentially generate an arc instability in the next layer, causing further flaw formation.

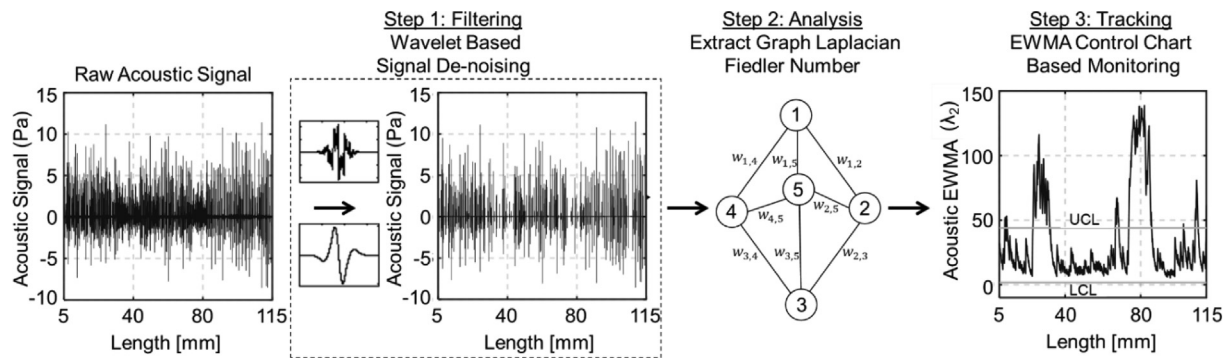


**Fig. 7.** Overview of the approach used for flaw detection. (1) The first step is filtering out the noise from the acoustic sensor data using wavelet analysis. (2) Next graph theory analysis is used to extract process signatures (Fiedler number). (3) The Fiedler number is then tracked using an EWMA control chart.

- b. Ability to operate on signals with sharp discontinuities (spikes), such as those characteristic of the WAAM process.

In this work, a discrete wavelet transform (DWT) is used to filter the raw acoustic signal ( $S$ ), which is derived from the continuous wavelet transform (CWT) shown in Eqn.(1) [46]:

$$W(a, b) = \frac{1}{\sqrt{a}} \int_{t=0}^{t=\infty} \bar{\psi} \left( \frac{t-b}{a} \right) S(t) dt \quad (1)$$

In Eqn.(1),  $a$  is the time dilation and  $b$  is the time translation of the analyzing wavelet ( $\bar{\psi}$ ). For the discrete acoustic signal used in this work, the DWT is derived from the CWT as:

$$W(2^i, 2^i n) \triangleq \frac{1}{\sqrt{2^i}} \sum_{d=1}^{d=N} \bar{\psi} \left( \frac{d}{2^i} - n \right) S(d) \quad (2)$$

Where  $d$  is the discrete data point and  $N$  is the total number of data points in the signal ( $S$ ). For the DWT, the time dilation and translation are set at the discrete values of  $2^i$  where  $i$  is the octave (or frequency level) being analyzed. For the purposes of this work,  $n = 1$  is selected to make the change from each octave more consistent and easier to interpret by keeping the time translation the same as the time dilation. This set time dilation and translation

is standard for basic wavelet analysis [47]. The DWT is used to deconstruct the signal into its base frequencies (octaves). The frequencies contaminated with background noise are identified and subsequently filtered from the signal.

Lastly the Discrete Inverse Wavelet Transform (DIWT) is used to reconstruct the base frequencies into a single de-noised signal ( $S_d$ ). The DIWT takes each deconstructed signal and performs a convolution to perform this reconstruction process. This allows for the de-noised signal to be analyzed and subsequently perform flaw detection.

This wavelet filtering process is summarized in Fig. 8 through Fig. 10. Referring to Fig. 8, the original signal ( $S$ ) is first divided between the first octaves ( $i = 1$ ) detailed ( $D$ ) and adjusted ( $A$ ) components of the signal. The detailed signal is representative of the particular data in that octave, and the adjusted signal is the remainder of the signal that did not fit the parameters of the wavelet at that octave. Thus, the signal is decomposed, using a deconstruction wavelet, in the first octave to obtain a detailed ( $D_1$ ) and adjusted ( $A_1$ ) components of the signal. In this work, a biorthogonal 3.3 wavelet is used to deconstruct and reconstruct the signal based on extensive offline studies [48]. The biorthogonal 3.3 wavelet was selected after extensive offline optimization not reported in this work. This wavelet package was advantageous for suppressing background noise without occluding relevant process signatures.

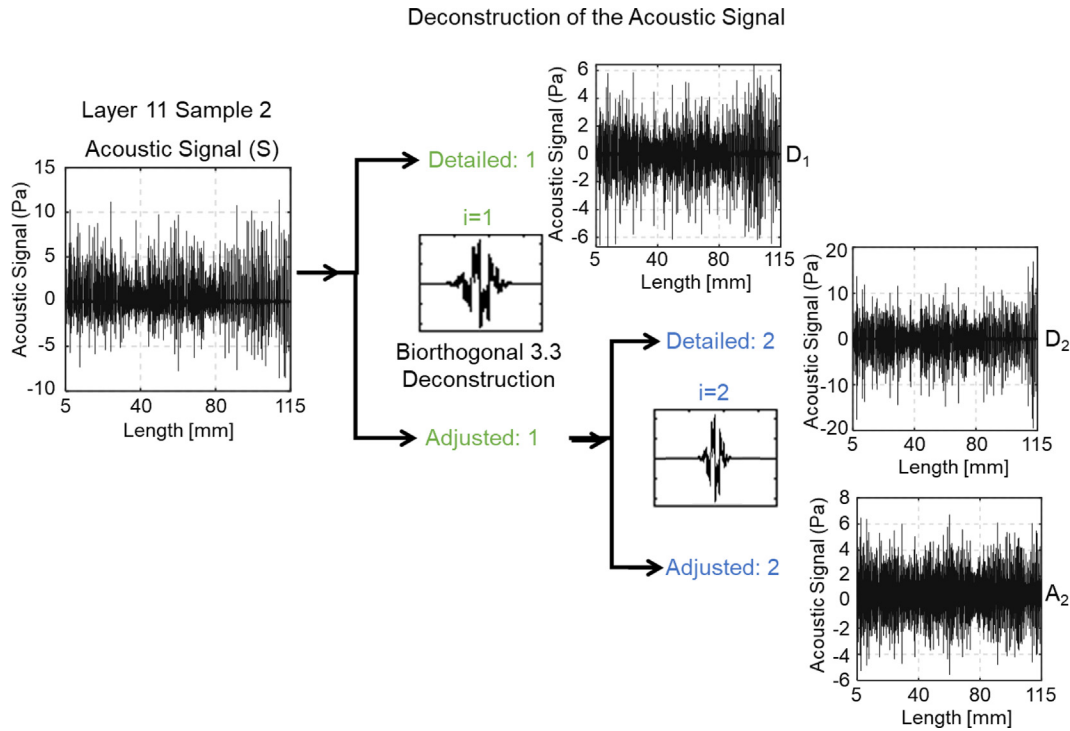


**Fig. 8.** Example of decomposing the raw signal (S) using the DWT (biorthogonal 3.3 wavelet). The detailed (D) and Adjusted (A) components over two octaves.

Next, the adjusted signal of the first octave ( $A_1$ ) undergoes another decomposition, into the detailed signal at the second octave ( $D_2$ ) and the adjusted signal ( $A_2$ ) at the second octave. This process can continue for several octaves. In this work 8 octaves are used, due to the signal losing intensity after 8 octaves. For each octave, the frequency regime of the detailed signal is essentially double of the previous octave due to the time translation and dilation of the deconstruction wavelet being a function of  $2^i$ . Hence, the signal (S) is decomposed into  $i$  number of detailed (D) and adjusted (A) components.

Referring to Fig. 9, once the signal is decomposed into  $i$  octaves and the adjusted signal, each octave is subject to a hard threshold. The hard threshold removes noise at each octave from the signal. In this work, these limits are determined heuristically. The eleventh layer of Sample 2 is chosen as the training layer due its visually distinctive changes between the signal, contamination, other flaws, and noise. Once the threshold levels are set based on data from layer 11, the thresholding limits are kept constant for all three samples and are not changed [49].

It is important to note that the adjusted signal,  $A_2$ , in the example in Fig. 9, does not have any threshold or filtering. This is because it does not represent any specific frequency and is the 'remainder' of all the data not already deconstructed into a base frequency.

Lastly, shown in Fig. 10, after the noise from each octave is removed the signal (S) is reconstructed back using the discrete inverse wavelet transform (DIWT), using a reconstruction wavelet ( $\bar{\psi}$ ) at each octave [12]. The reconstruction process results in a de-noised signal ( $S_d$ ). The de-noised signal ( $S_d$ ) manifests the process dynamics in a distinctive manner. For example, in Fig. 10, the de-noised signal has a decrease in amplitude corresponding to the introduction of oil, which is not evident in the raw acoustic signal (Fig. 5(b)).

This wavelet deconstruction and reconstruction approach is applied to the acoustic signal for all three samples. The wavelet

type, number of octaves used, and the thresholding limits are summarized in Table 3. The biorthogonal 3.3 wavelet has a deconstruction and reconstruction component, shown in Fig. 8 and Fig. 10 respectively.

### 3.2. Step 2 - signal analysis

#### 3.2.1. Data extraction

After wavelet analysis, the de-noised acoustic signal ( $S_d$ ) is analyzed in the graph domain, and a single number called the Fiedler number ( $\lambda_2$ ) is obtained. The Fiedler number is then used as the monitoring statistic for detecting flaw formation. This approach circumvents extraction of several statistical features from the sensor data for process monitoring, and is therefore computationally efficient.

First, the de-noised signal ( $S_d$ ) is sampled into  $k$  number of windows, each window having a length of  $N$  data points. For spatial resolution and physical relevance, 10 windows per millimeter of a deposited track are imposed. This results in 1200 windows per layer with 512 data points per window, as detailed in Fig. 11. The 512 data points ( $N$ ) translates to 0.02 s of data collection (or 0.1 mm deposition). From each window the Fiedler number ( $\lambda_2$ ) is obtained and tracked using an exponentially weighted moving average (EWMA) control chart. The process for obtaining the Fiedler number ( $\lambda_2$ ) is described in the following steps, and the relevance is discussed by Ref. [13].

#### 3.2.2. Creation of network graph

A network graph is created from the 512 data points in each  $k$  window. Given a 1-D signal ( $S_d^{512 \times 1}$ ), the network graph contains 512 nodes. Each node  $i$ , is connected to node  $j$ , by an edge  $w(i,j)$  whose weight is the Euclidean distance ( $L_2$  Norm) between the two nodes detailed in Eqn.(3):

$$w(i,j) = \|S_d(i) - S_d(j)\|_2 = |S_d(i) - S_d(j)| \quad (3)$$



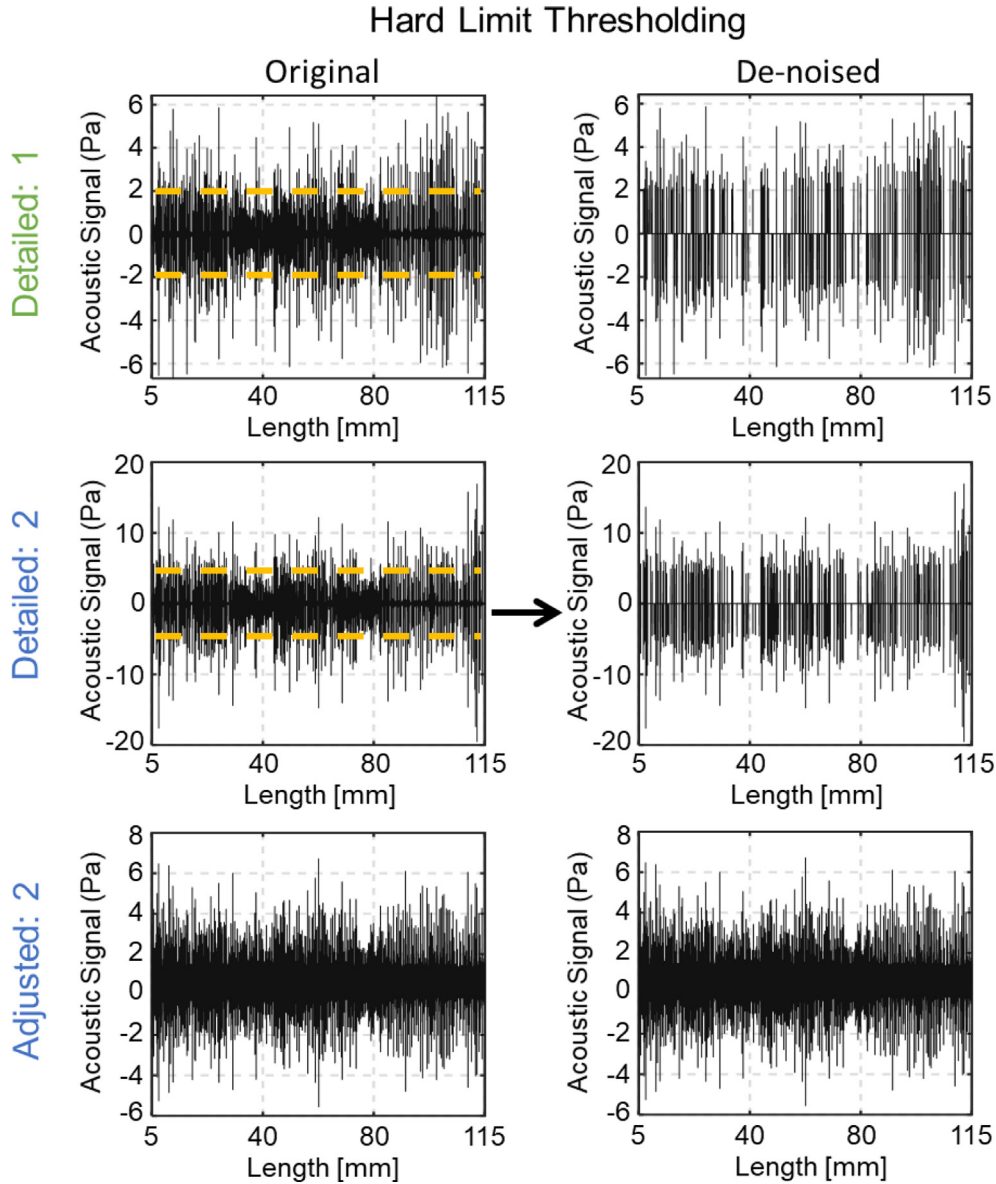


**Fig. 9.** Hard limit thresholding used to de-noise each detailed component. The orange dashed lines represent the location of thresholding used to remove extraneous noise.

Where  $S_d(i)$  is the amplitude of the de-noised acoustic signal ( $S_d$ ) at node  $i$ . The Euclidean distances  $w(i,j)$  result in a weighted adjacency matrix ( $W_k$ ) for each window  $k$ . Next the weighted adjacency matrix is translated into a sparse adjacency matrix ( $H_k$ ) where all edge values of  $W_k$  are converted to 1's and 0's based on a threshold ( $\varepsilon$ ) as detailed in Eqn.(4):

$$h(i,j) = \begin{cases} 1, & w_k(i,j) > \varepsilon \\ 0, & w_k(i,j) \leq \varepsilon \end{cases} \quad (4)$$

The threshold  $\varepsilon$  is not fixed, but is estimated from the data, and changes for each window. The threshold value ( $\varepsilon$ ) is the combined average node weight of the current window and the previous 5 windows ( $\beta = 5$ ). The Euclidean distance of the previous  $\beta = 5$  windows is chosen as it corresponds physically to 0.5 mm of the track deposited. This allows for the system to be more flexible to global fluctuations and reduce the number of false alarms. The distance of 0.5 mm was chosen as it is half the width of the  $\sim 1$  mm diameter holes in which the contaminants were placed. The visual representation of this process is shown in Fig. 11, and the threshold  $\varepsilon$  is calculated as:

$$\varepsilon = \frac{\sum_{k=\beta}^K \left[ \frac{\sum W_k}{N} \right]}{\beta + 1} \quad (5)$$

From the sparse adjacency matrix ( $H_k$ ), the Laplacian matrix ( $\mathcal{L}_k$ ) is calculated for each window as follows [50]:

$$\mathcal{L}_k = D_k - H_k \quad (6)$$

Where the degree matrix ( $D_k$ ) is the diagonal sum of the sparse adjacency matrix:

$$D_k(i,i) = \sum_{i=1}^i H_k(i,i) \quad (7)$$

Finally, the eigenspectra Laplacian matrix ( $\mathcal{L}_k$ ) for each window  $k$  is obtained, where  $\lambda$  are the eigenvalues and  $v$  are the eigenvectors [50]:

$$\mathcal{L}_k v = \lambda v \quad (8)$$

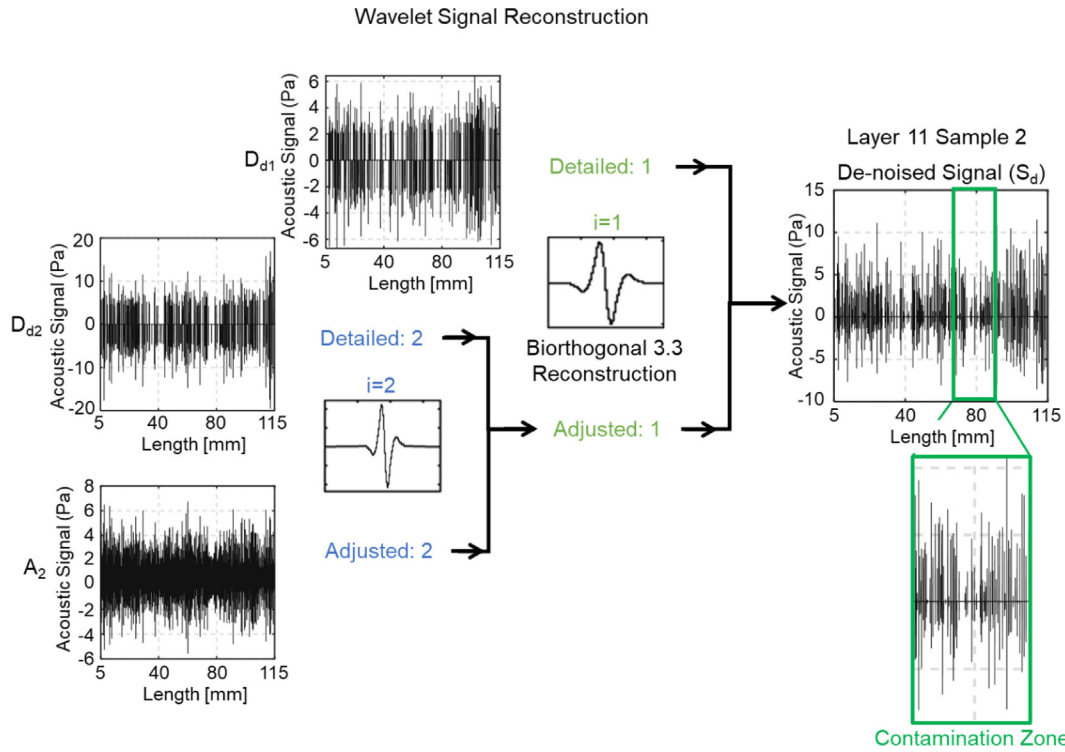


**Fig. 10.** Reconstruction of the de-noised signal using the DIWT. The filtered detailed (D) and adjusted (A) signal are combined using a reconstruction (biorthogonal 3.3) wavelet.

**Table 3**  
Thresholding parameters used in the Wavelet Filtering process.

Biorthogonal 3.3 Octaves	Octave 1	Octave 2	Octave 3	Octave 4	Octave 5	Octave 6	Octave 7	Octave 8
Thresholding Limits	$\pm 2.002$	$\pm 4.081$	$\pm 4.670$	$\pm 3.159$	$\pm 3.582$	$\pm 2.812$	$\pm 3.150$	$\pm 3.448$

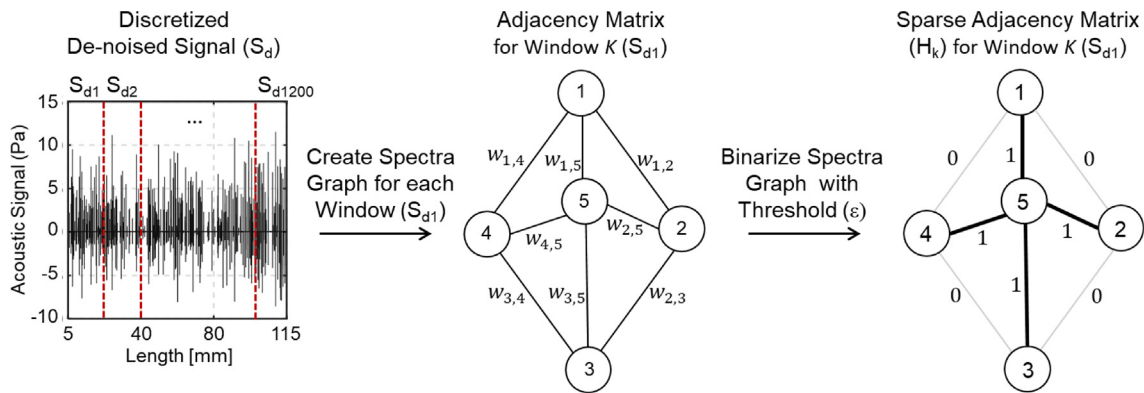


**Fig. 11.** Visual representation of converting the de-noised signal  $S_{d1}$  into the adjacency matrix and then the sparse adjacency matrix ( $H_k$ ). The dashed red lines represent each discrete window. There are 1200 windows per layer in the de-noised signal ( $S_d$ ).

The second eigenvalue ( $\lambda_2$ ) and eigenvector ( $v_2$ ) are called the Fiedler number ( $\lambda_2$ ) and Fiedler vector ( $v_2$ ) respectively. The Fiedler number ( $\lambda_2$ ) for each window is the monitoring statistic used for the process. The analysis results in 1200 Fiedler numbers ( $\lambda_2$ ) per layer where there are 10 Fiedler numbers per 1 mm, 1 Fiedler number for every window. The mathematical properties of the Fiedler number are described in depth in Ref. [13]. Thus, the process dynamics contained in the acoustic data is encompassed in one statistic, the Fiedler number ( $\lambda_2$ ), in place of several statistical features.

### 3.3. Step 3 - process monitoring (Tracking)

To determine when an arc instability occurs, the Fiedler numbers ( $\lambda_2$ ) from the signal are tracked using an exponentially weighted moving average (EWMA) statistical control chart [51]. This approach eschews the complex machine learning for flaw monitoring, and is readily implemented in a practical environment.

In an EWMA control chart, the process is deemed to be out-of-control when the signal crosses a control limit. In this work, an out-of-control condition is indicative of an arc instability and impending

ing flaws. The EWMA control chart plots the statistic  $Z_k$  for a given data point at instant  $k$ ,  $Z_k$  is calculated as:

$$Z_k = \alpha \lambda_{2,k} + (1 - \alpha) Z_{k-1} \quad (9)$$

Where  $\lambda_{2,k}$  is the Fiedler number for the  $k^{\text{th}}$  window and Eqn.(9) is recursive with respect to  $Z_k$ . Traditionally the weight ( $\alpha$ ) has a value between 0.1 and 0.3, meaning that the new data point is being weighted only 10–30 % of its actual value. The higher the sampling rate the smaller  $\alpha$  should be to account for stochastic fluctuations and reduce noise, in this work, we set  $\alpha = 0.1$  [51]. The control limits are determined from nominal fault-free conditions found on layers 8 and 9 of Sample 3 (the sample with the least flaws observed). Thus, the control limits are estimated when there are no special fluctuations in the process and no observable flaws in the part. The upper control limit (UCL) and lower control limit (LCL) are found using the following Eqn.(10) [14]:

$$\text{UCL, LCL} = \mu_0 \pm \tau * \sigma_0 \sqrt{\frac{\alpha}{2 - \alpha}} \quad (10)$$

Values  $\mu_0$  and  $\sigma_0$  are the mean and standard deviation of the nominal flaw free signal. Finally,  $\tau$  is the number of standard deviations expected in the signal before the system is considered out-of-control. Traditionally for stationary systems this value is approximately  $\tau = 3$  [52]. However, given that the current system is non-stationary and nonlinear, the  $\tau$  value is increased significantly in this work so that  $\tau = 10$ . With this information, the UCL and LCL are determined to be 44 and 1.5, respectively. Using these control limits for the EWMA control chart results in a control Average Run Length ( $ARL_0$ ) of 62 [53]. This is calculated from layers 8 and 9 from Sample 3, consisting of 2,200 samples, which are the same flaw free layers used to calculate the control limits. With the reported  $ARL_0$  of 62, the false alarm rate is approximately 1.6 % or 3 false alarms every 200 samples visualized in Fig. 12. This false alarm rate is on par with those reported in the AM literature, both in other DED based research [54] (less than 2.1 %), and in the more thoroughly researched LPBF process [55,56] (between 0.6 % and 9%).

## 4. Results

### 4.1. Flaw detection at the layer level

#### 4.1.1. Detection of contamination

To demonstrate the detection of arc instabilities generated from contamination regions layer 11 of Sample 1, which contained two

chalk contamination zones (green), is shown in Fig. 13. The contamination zones disrupted the arc significantly and is evident in the de-noised signal ( $S_d$ ), as depicted in Fig. 13(a). These contamination zones resulted in two prominent line width variations shown in Fig. 13(b), which was found in the post process characterization of the XCT analysis. This layer also contains a line width variation at the start of the layer (purple) and a pore (red) approximately 115 mm along the part that is not evident in the de-noised acoustic signal. Detection of porosity and line width variation are presented in Case 2 (Sec. 4.1.2), and Case 3 (Sec. 4.1.3), respectively. However, all flaws are apparent in Fig. 13(c), when the control statistic crosses the upper control limit.

#### Case 2 Detection of Porosity.

To demonstrate the ability to detect porosity, layer 1 of Sample 3 is shown in Fig. 14. The de-noised acoustic signature is shown in Fig. 14(a). In the corresponding XCT slice shown in Fig. 14(b), two pores located at ~ 5 & 110 mm along the length of the layer. The two pores are clearly detected on the EWMA control chart in Fig. 14(c). In this layer, significant line width variation is observed along with intermittent spikes across the control limit in the corresponding regions. Detection of line width variation will be further detailed in Case 3 (Sec. 4.1.3).

#### Case 3 Detection of Line Width Variation and Spatter.

Shown in Fig. 15 is the signal analysis for layer 7 of Sample 1 where the two chalk contamination regions created significant line width variations (purple-marked regions). As demarcated in the

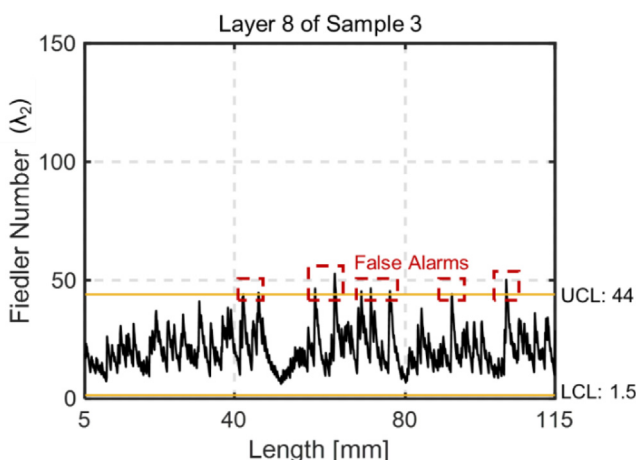


Fig. 12. Visualization of the false alarm rate ( $ARL_0$ ) in a fault-free layer (layer 8) in Sample 3. The  $ARL_0$  is 62 or 1.6%, or 3 false alarms every 200 samples.

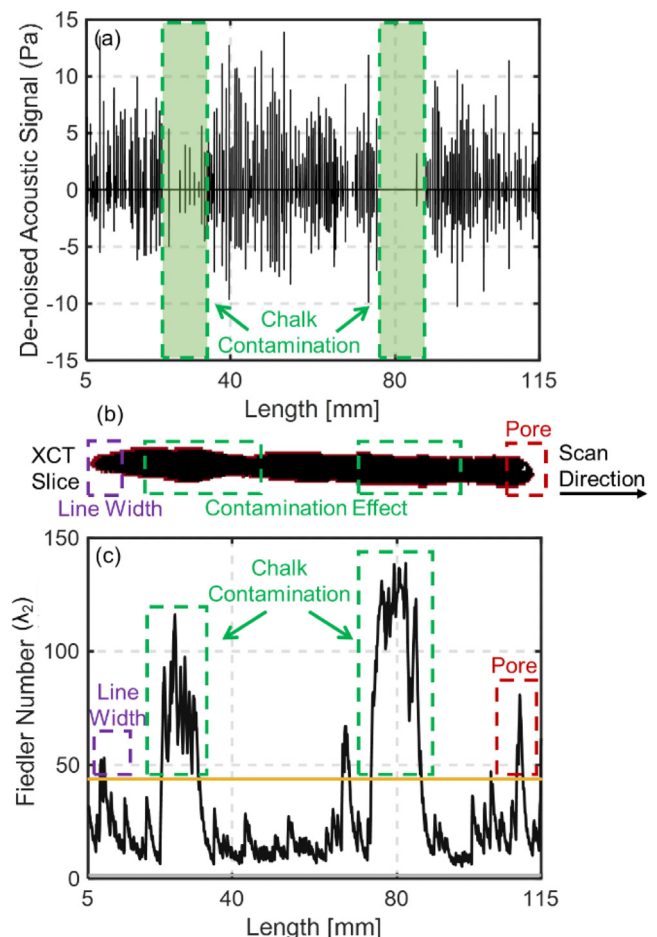
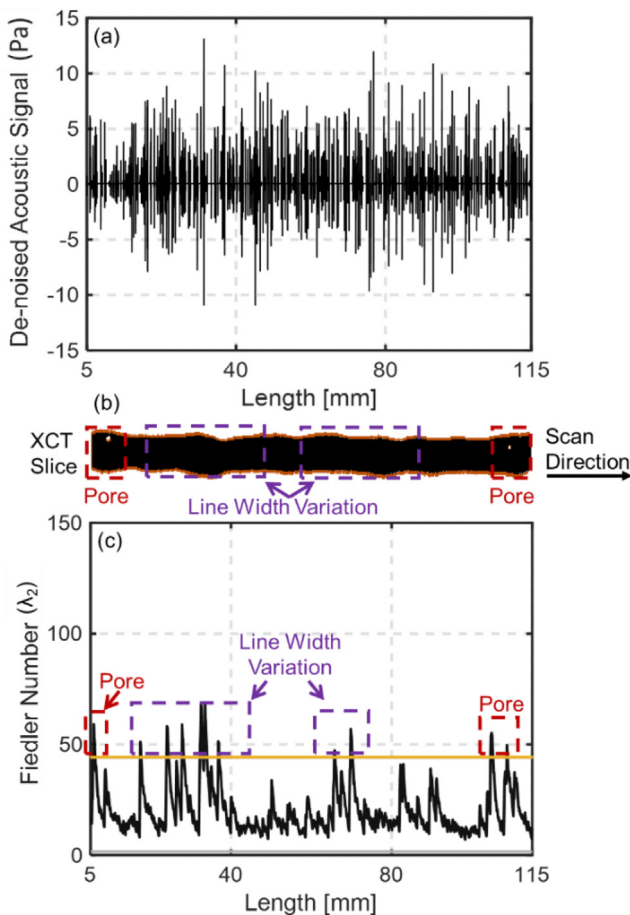


Fig. 13. (a) De-noised signal of layer 11 Sample 1 containing chalk contamination. (b) Line width variations are apparent in the XCT slice of this layer. (c) Line width variation caused by Contamination (green) crosses the upper control limit in the EWMA control chart.



**Fig. 14.** (a) De-noised signal of layer 1 Sample 3 containing no contamination. (b) Two pores on the edge (red) are apparent in the XCT slice of this layer. (c) Porosity causes the signal to cross the upper control limit in the EWMA control chart (red).

de-noised acoustic signal of Fig. 15(a), the two contamination regions at the 40 and 80 mm points forces a slight decay in the acoustic signal. These contamination zones did not create any porosity, however the entirety of layer 7 is afflicted with line width variations along with satellites due to spatter, as evidenced in the XCT slice of Fig. 15(b). The result of arc instabilities is not evident in the de-noised acoustic signal, Fig. 15(a), but can be observed in the EWMA control chart in Fig. 15(c). The start of layer 7 also had two small spikes above the EWMA control limit that were not correlated to a specific defect in the part and are counted as false alarms. These are labeled as uncorrelated detections and are discussed in greater detail in Sec. 4.2.

#### Case 4 Detection of Multiple Flaws in a Layer.

To demonstrate the detection of all the previously discussed flaws (porosity, line width variation, spatter), Fig. 16(a) shows the raw signal for layer 11 of Sample 2. Layer 11 has two contamination zones that led to large pores at 40 and 80 mm, along with a third pore at the end of the layer observed in Fig. 16(b). Also evident in the XCT slice are large line width variations at the start of the layer, and narrowing of the width between the two contamination regions, and immediately after the second contamination zone. For a comparison, Fig. 16(c) shows the EWMA control chart tracking the Fiedler number ( $\lambda_2$ ). The two large pores resulting from the oil contamination and are clearly detected by large spikes past the control limit in the control chart at 40 and 80 mm.

Three line width variations are also evident in the layer demarcated in Fig. 16(b). The first line width change is at the beginning of the layer. Then, the next line width variation is after the first pore

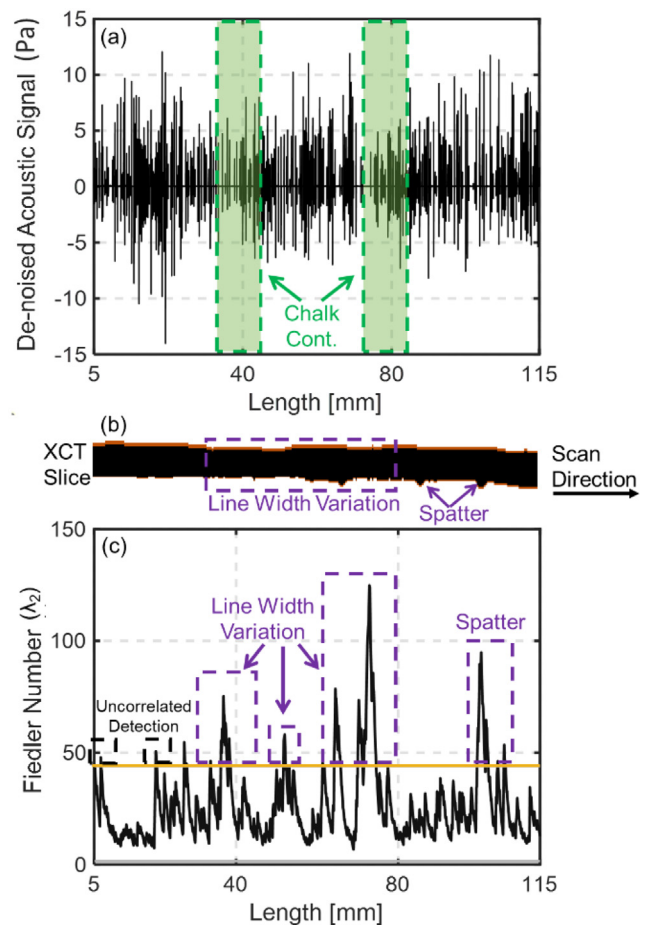


**Fig. 15.** (a) De-noised signal of layer 7 Sample 1 containing chalk contamination. (b) Line width variation and spatter satellites (purple) are apparent in the XCT slice of this layer. (c) These variations are detected when the signal crosses the upper control limit in the control chart.

(created due to contamination) when the arc is stabilizing, and the final variation is a 'pinch point' immediately after pore located at 80 mm. The pore located near 110 mm is clearly detected by another large spike in the control chart.

#### 4.2. Layer-by-Layer detection

To observe and detect arc instability on a layer-by-layer basis, the total number of out-of-control points are counted per layer of the EWMA control chart. The number of out-of-control points are subsequently correlated to the number of flaws observed in that layer from XCT. The application of this analysis is shown in Fig. 17.

In Sample 1, corresponding to Fig. 17(a), the majority of out-of-control points (arc instability) occur between layer 7 and layer 11 which contained the contamination zones (green). In these layers, severe porosity (red) and line width variation flaws (purple) are found from the XCT analysis. Layer 2 contains a large number of out-of-control detection and are correlated to the two pores created in the previous layer. Sample 1 depicts a total over 1,000 out-of-control detections and corresponding flaws. In comparison, Sample 3, detailed in Fig. 17(c), contained only 343 out-of-control and had very few generated flaws.

For Sample 2, it is observed that the majority of out-of-control points occurred on the second half of the build, as depicted in Fig. 17(b). When correlated to the physical part (Sample 2), the



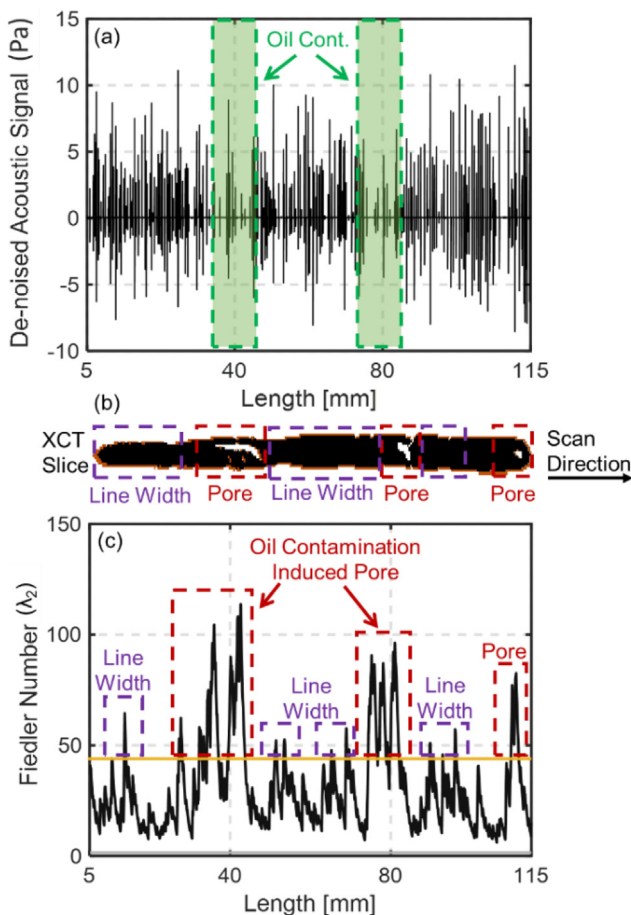


**Fig. 16.** (a) De-noised signal of layer 11 Sample 2 containing oil contamination. (b) Two voids caused by contamination (green), line width variation (purple), and porosity (red) are apparent in the XCT slice of this layer. (c) All of these flaws are accurately detected in the control chart.

majority of the visual spatter begins to accumulate on layer 7. This is also where significant line width variations are observed in the part. Additionally, the majority of pores in Sample 2 are contained to layer 7 and layer 11 where oil contamination is introduced. The total number of arc instabilities observed in Sample 2 is 1,991, which is significantly more than the 343 detections found in Sample 3.

Fig. 17(c) shows the comparison of the number of out-of-control points detected and generated flaws for Sample 3. Minimal number of faults are detected at layer 7 or 11 where sand contamination is introduced compared to chalk (Sample 1) and oil (Sample 2). Layer 1 of Sample 3 depicts line width variation and porosity, and has the second highest level of arc instability detections. Another high number of out-of-control points are observed in layer 10 which contains 2 small pores. In total, Sample 3 has minimal flaws generated in comparison to Sample 1 and 2 and has significantly fewer out-of-control detections. Additionally, the number of arc instability detections could also provide an indication of overall quality of the part. For example, on finding the number of arc instability detections to be above a certain threshold, an operator can stop the process.

In all three samples there are out-of-control detections that did not directly correlate to flaw formation and are indicated with the label of 'uncorrelated detection' in Fig. 17. All layers had some level of line width variations and potentially related to these uncorrelated detections. These uncorrelated detections are encompassed in the false positive rate of 1.6 % as discussed in Sec. 3.3. A limita-

tion of this work is that it is focused on detecting arc instability and not specific types of flaws resulting from arc instability (Fig. 6). We reiterate that using the method proposed in this work, it is to determine the occurrence of an incipient flaw and its location as a result of an arc instability, however, the approach cannot stratify and distinguish between the different types of flaws.

## 5. Conclusions and future work

In this work we developed and applied an approach for flaw monitoring during the wire arc additive manufacturing (WAAM) process using data acquired from an in-situ acoustic sensor. The approach integrates wavelet-based signal filtering with a novel spectral graph signal analysis technique to monitor process faults, such as arc instabilities. This is a valuable contribution, because, thus far process monitoring in WAAM has been largely restricted to tracking process-level variables, such as voltage and current. Instead, the approach presented in this work is focused on detecting causal part-level phenomena, such as arc instabilities that are symptomatic of incipient flaw formation.

Moreover, the sensor used in this work is an acoustic (sound) sensor which is relatively inexpensive compared to infrared thermal cameras and pyrometers used in the current literature. Lastly, the graph theory signal analysis involved extraction of only one signature (feature) from the acoustic signature called the graph Laplacian Fiedler number ( $\lambda_2$ ). This Fiedler number is subsequently tracked in a readily interpretable statistical control chart. The approach has two key advantages: (i) it eschews extensive signal processing and black-box machine learning, and instead relies on a simple and intuitive univariate control chart to detect flaw formation, (ii) A single monitoring statistic, i.e.,  $\lambda_2$ , is extracted and used for flaw monitoring in place of an array of statistical features. Consequently, the approach is both practitioner-friendly and computationally tractable. Specific conclusions from the work are as follows:

- (1) We deposited three WAAM parts (stainless steel 316L). Each of these parts had arc instabilities induced by introducing three types of contaminants at specific layers. The three types of contamination were chalk, oil, and sand, which resulted in arc instabilities of varying intensities. These arc instabilities in turn resulted in flaws such as porosity, variation in the line width, and spatter which were identified from post-process XCT of the parts.
- (2) During the deposition process, acoustic signals were acquired by a Shure SM57 microphone installed in close proximity to the welding torch. The microphone translates with the nozzle, hence its position with respect to the arc is constant. Data is acquired continuously at a sampling rate of 25.6 kHz continuously during the process.
- (3) A three-step approach is developed to process the acoustic signal and consequently pinpoint the location on the layer at which a flaw is likely to occur. The first step is to filter the extraneous noise in the acoustic sensor data using a wavelet decomposition approach. The second step focuses on extracting relevant features from the filtered data that are sensitive to flaw formation. In this work, we used a graph theory-based approach to analyze the data and consequently extract a single feature – the second graph Laplacian eigenvalue called the Fiedler number ( $\lambda_2$ ). In the third step, the Fiedler number is tracked in a readily implemented control chart called the exponentially weighted moving average (EWMA) control chart. The control limits of the chart were tuned such that the false alarm rate (type 1 error) was 1.6 %.

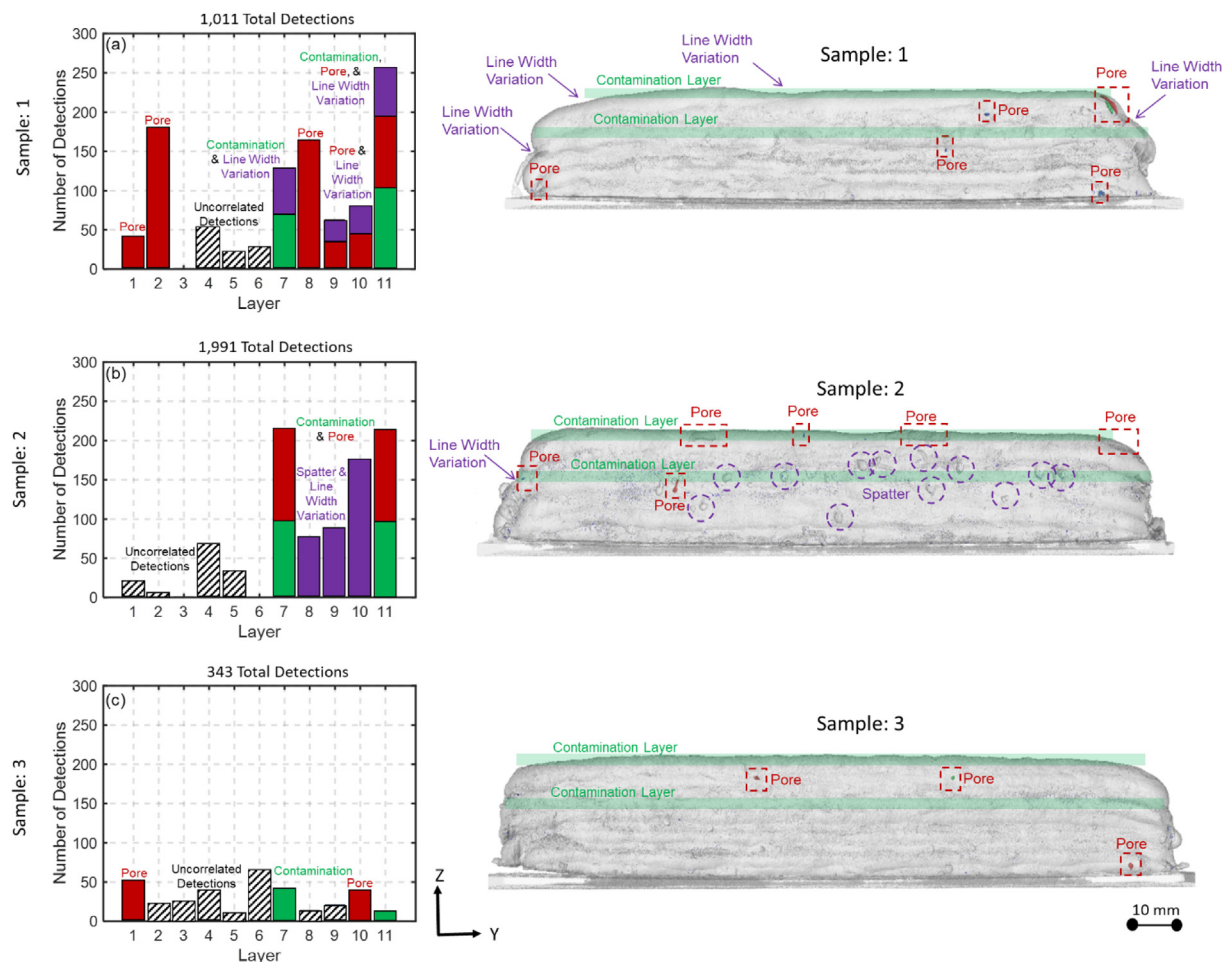


**Fig. 17.** Comparison between all three samples and the number of arc instability detections in each layer. (c) Sample 3 had both the fewest number of arc detections and the fewest flaws. In comparison to (a) Sample 1 and (b) Sample 2 which had over 1,000 detections and significant number of flaws.

- (4) The approach accurately detects the formation of various types of flaws, such as line width variation, voids created due to contamination, porosity, and spatter formation on the part.

In our future work we will endeavor to further improve upon the practical scalability of the approach by integrating multiple sensors for process monitoring, such as thermal and laser point cloud scanning. With the assistance of the other sensors installed in the machine, the goal is to not only detect the onset of flaw formation, but also, to identify the specific type of flaw formed as a result of arc instability, and subsequently correct the flaw through feedback control. An initial feedback control algorithm can be developed with the approach described in this manuscript, by simply counting the number of arc instabilities per layer. If number of arc instabilities detected in a layer were to exceed a certain threshold, then the layer is removed via CNC milling and then re-deposited. Furthermore, our forthcoming work, will elucidate the effect of thermal history of the part on flaw formation, as opposed to only arc instability. This approach will also be validated with large-scale WAAM parts, then generalized to work with materials other than stainless steel 316L, and other WAAM machines.

#### Data availability

Data will be made available on request.

#### Declaration of Competing Interest

The authors declare that they have no known competing financial interests or personal relationships that could have appeared to influence the work reported in this paper.

#### Acknowledgments

André Ramalho acknowledges Fundação para a Ciência e a Tecnologia (FCT-MCTES) for funding the Ph.D. Grant UI/BD/151018/2021. André Ramalho, Telmo G. Santos and J.P. Oliveira acknowledge Fundação para a Ciência e a Tecnologia (FCT-MCTES) for its financial support via the project UID/00667/2020 (UNIDEMI). J. P. Oliveira acknowledges funding by national funds from FCT - Fundação para a Ciência e a Tecnologia, I.P., in the scope of the projects LA/P/0037/2020, UIDP/50025/2020 and UIDB/50025/2020 of the Associate Laboratory Institute of Nanostructures, Nanomodelling and Nanofabrication – i3N. This activity has received funding from the European Institute of Innovation and Technology (EIT) – Project Smart WAAM: Microstructural Engineering and Integrated Non-Destructive Testing. This body of the European Union receives support from the European Union's Horizon 2020 research and innovation program.

Prahalada Rao acknowledges funding from the Department of Energy (DOE), Office of Science, under Grant number DE-SC0021136, and the National Science Foundation (NSF) [Grant numbers CMMI-1719388, CMMI-1920245, CMMI-1739696,

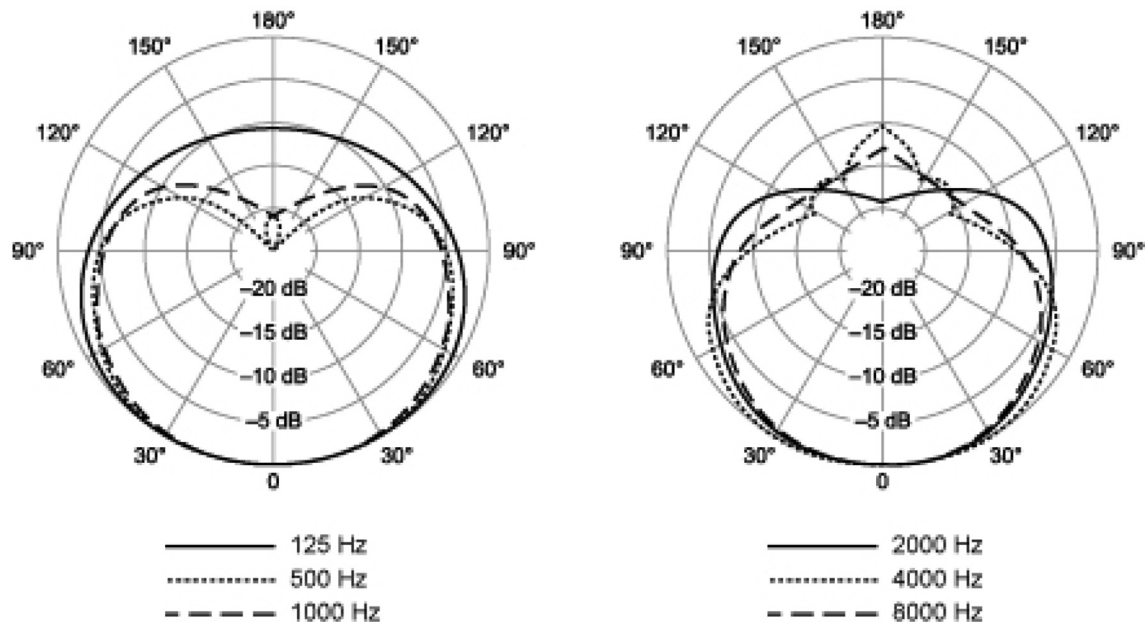


Fig. 18. Polarity pattern for the Shure SM57 acoustic microphone.

CMMI-1752069, PFI-TT 2044710, ECCS 2020246] for funding his research program. This work espousing the concept of online process monitoring in WAAM was funded through the foregoing DOE Grant (Program Officer: Timothy Fitzsimmons), which partially supported the doctoral graduate work of Mr. Benjamin Bevans at University of Nebraska-Lincoln Benjamin, Aniruddha, and Ziyad Smoqi were further supported by the NSF grants CMMI 1752069 (CAREER) and ECCS 2020246. Detecting flaw formation in metal AM using in-situ sensing and graph theory-based algorithms was a major component of CMMI 1752069 (program office: Kevin Chou). Developing machine learning algorithms for advanced manufacturing applications was the goal of ECCS 2020246 (Program officer: Donald Wunsch). The XCT work was performed at the Nebraska Nanoscale Facility: National Nanotechnology Coordinated Infrastructure under award no. ECCS: 2025298, and with support from the Nebraska Research Initiative through the Nebraska Center for Materials and Nanoscience and the Nanoengineering Research Core Facility at the University of Nebraska-Lincoln. The acquisition of the XCT scanner at University of Nebraska was funded through CMMI 1920245 (Program officer: Wendy Crone).

## Appendix

Shure SM57 Acoustic Microphone polarity patterns are shown below Fig. 18.

## References

- [1] A. Dass, A. Moridi, State of the art in directed energy deposition: From additive manufacturing to materials design, *Coatings* 9 (2019) 418, <https://doi.org/10.3390/coatings9070418>.
- [2] D.-G. Ahn, Directed Energy Deposition (DED) Process: State of the Art, *International Journal of Precision Engineering and Manufacturing-Green Technology* 8 (2021) 703–742, <https://doi.org/10.1007/s40684-020-00302-7>.
- [3] C. Xia, Z. Pan, J. Polden, H. Li, Y. Xu, S. Chen, Y. Zhang, A review on wire arc additive manufacturing: Monitoring, control and a framework of automated system, *J. Manuf. Syst.* 57 (2020) 31–45, <https://doi.org/10.1016/j.jmsy.2020.08.008>.
- [4] S.R. Singh, P. Khanna, Wire arc additive manufacturing (WAAM): A new process to shape engineering materials, *Mater. Today: Proc.* 44 (2021) 118–128, <https://doi.org/10.1016/j.matpr.2020.08.030>.
- [5] D. Ding, S. Zhang, Q. Lu, Z. Pan, H. Li, K. Wang, The well-distributed volumetric heat source model for numerical simulation of wire arc additive manufacturing process, *Mater. Today Commun.* 27 (2021), <https://doi.org/10.1016/j.mmtcomm.2021.102430> 102430.
- [6] A. Nycz, M.W. Noakes, B.S. Richardson, A.K. Messing, B.K. Post, J.H. Paul, J. Flamm, L.J. Love, Challenges in Making Metal Large-scale Complex Parts for Additive Manufacturing: A Case Study Based on the Additive Manufacturing Excavator (AME), Oak Ridge National Lab.(ORNL), Oak Ridge, TN (United States), 2017.
- [7] Y. Li, Q. Han, I. Horváth, G. Zhang, Repairing surface defects of metal parts by groove machining and wire + arc based filling, *J. Mater. Process. Technol.* 274 (2019), <https://doi.org/10.1016/j.jmatprotec.2019.116268> 116268.
- [8] F. Xu, V. Dhokia, P. Colegrove, A. McAndrew, S. Williams, A. Henstridge, S.T. Newman, Realisation of a multi-sensor framework for process monitoring of the wire arc additive manufacturing in producing Ti-6Al-4V parts, *Int. J. Comput. Integr. Manuf.* 31 (2018) 785–798, <https://doi.org/10.1080/0951192X.2018.1466395>.
- [9] B. Wu, Z. Pan, D. Ding, D. Cuiuri, H. Li, J. Xu, J. Norrish, A review of the wire arc additive manufacturing of metals: properties, defects and quality improvement, *J. Manuf. Process.* 35 (2018) 127–139, <https://doi.org/10.1016/j.jmapro.2018.08.001>.
- [10] A. Ramalho, T.G. Santos, B. Bevans, Z. Smoqi, P. Rao, J.P. Oliveira, Effect of contaminations on the acoustic emissions during wire and arc additive manufacturing of 316L stainless steel, *Addit. Manuf.* 51 (2022), <https://doi.org/10.1016/j.addma.2021.102585> 102585.
- [11] A. Thompson, I. Maskery, R.K. Leach, X-ray computed tomography for additive manufacturing: a review, *Meas. Sci. Technol.* 27 (2016) 72001, <https://doi.org/10.1088/0957-0233/27/7/072001>.
- [12] D.M.H. and J.L. Yansun Xu, J. B. Weaver, Wavelet transform domain filters: a spatially selective noise filtration technique, *IEEE Transactions on Image Processing* 3 (1994) 747–758. <https://doi.org/10.1109/83.336245>.
- [13] M.S. Tootooni, P.K. Rao, C. Chou, Z.J. Kong, A Spectral Graph Theoretic Approach for Monitoring Multivariate Time Series Data From Complex Dynamical Processes, *IEEE Trans. Autom. Sci. Eng.* 15 (2018) 127–144, <https://doi.org/10.1109/TASE.2016.2598094>.
- [14] V. do C.C. de Vargas, L.F. Dias Lopes, A. Mendonça Souza, Comparative study of the performance of the CuSum and EWMA control charts, *Computers & Industrial Engineering* 46 (2004) 707–724. <https://doi.org/10.1016/j.cie.2004.05.025>.
- [15] T.A. Rodrigues, V. Duarte, R.M. Miranda, T.G. Santos, J.P. Oliveira, Current Status and Perspectives on Wire and Arc Additive Manufacturing (WAAM), *Materials* 12 (2019), <https://doi.org/10.3390/ma12071121>.
- [16] X. Chen, F. Kong, Y. Fu, X. Zhao, R. Li, G. Wang, H. Zhang, A review on wire-arc additive manufacturing: typical defects, detection approaches, and multisensor data fusion-based model, *Int. J. Adv. Manuf. Technol.* 117 (2021) 707–727, <https://doi.org/10.1007/s00170-021-07807-8>.
- [17] C. Xia, Z. Pan, S. Zhang, J. Polden, L. Wang, H. Li, Y. Xu, S. Chen, Model predictive control of layer width in wire arc additive manufacturing, *J. Manuf. Process.* 58 (2020) 179–186, <https://doi.org/10.1016/j.jmapro.2020.07.060>.
- [18] M. Shi, J. Xiong, G. Zhang, S. Zheng, Monitoring process stability in GTA additive manufacturing based on vision sensing of arc length, *Measurement* 185 (2021), <https://doi.org/10.1016/j.measurement.2021.110001> 110001.



- [19] Q. Zhan, Y. Liang, J. Ding, S. Williams, A wire deflection detection method based on image processing in wire+ arc additive manufacturing, *Int. J. Adv. Manuf. Technol.* 89 (2017) 755–763.
- [20] S. Suryakumar, K.P. Karunakaran, A. Bernard, U. Chandrasekhar, N. Raghavender, D. Sharma, Weld bead modeling and process optimization in Hybrid Layered Manufacturing, *Comput. Aided Des.* 43 (2011) 331–344, <https://doi.org/10.1016/j.cad.2011.01.006>.
- [21] A. Richter, T. Gehling, K. Treutler, V. Wesling, C. Rembe, Real-time measurement of temperature and volume of the weld pool in wire-arc additive manufacturing, *Measurement: Sensors*. 17 (2021), <https://doi.org/10.1016/j.measen.2021.100060> 100060.
- [22] D. Yang, G. Wang, G. Zhang, Thermal analysis for single-pass multi-layer GMAW based additive manufacturing using infrared thermography, *J. Mater. Process. Technol.* 244 (2017) 215–224, <https://doi.org/10.1016/j.jmatprotec.2017.01.024>.
- [23] C. Zhang, M. Gao, C. Chen, X. Zeng, Spectral diagnosis of wire arc additive manufacturing of Al alloys, *Addit. Manuf.* 30 (2019), <https://doi.org/10.1016/j.addma.2019.100869> 100869.
- [24] T. Hauser, R.T. Reisch, P.P. Breese, Y. Nalam, K.S. Joshi, K. Bela, T. Kamps, J. Volpp, A.F.H. Kaplan, Oxidation in wire arc additive manufacturing of aluminium alloys, *Addit. Manuf.* 41 (2021), <https://doi.org/10.1016/j.addma.2021.101958> 101958.
- [25] K. Ito, M. Kusano, M. Demura, M. Watanabe, Detection and location of microdefects during selective laser melting by wireless acoustic emission measurement, *Addit. Manuf.* 40 (2021), <https://doi.org/10.1016/j.addma.2021.101915> 101915.
- [26] S.A. Shevchik, C. Kenel, C. Leinenbach, K. Wasmer, Acoustic emission for in situ quality monitoring in additive manufacturing using spectral convolutional neural networks, *Addit. Manuf.* 21 (2018) 598–604, <https://doi.org/10.1016/j.addma.2017.11.012>.
- [27] D. Kouprianoff, I. Yadroitsava, A. du Plessis, N. Luwes, I. Yadroitsev, Monitoring of Laser Powder Bed Fusion by Acoustic Emission: Investigation of Single Tracks and Layers, *Frontiers in Mechanical Engineering*. 7 (2021) 60.
- [28] Z. Liang, L. Jinglong, L. Yi, H. Jingtao, Z. Chengyang, X. Jie, C. Dong, Characteristics of metal droplet transfer in wire-arc additive manufacturing of aluminum alloy, *Int. J. Adv. Manuf. Technol.* 99 (2018) 1521–1530, <https://doi.org/10.1007/s00170-018-2604-7>.
- [29] A.M. Pringle, S. Oberloier, A.L. Petsiuk, P.G. Sanders, J.M. Pearce, Open source arc analyzer: Multi-sensor monitoring of wire arc additive manufacturing, *HardwareX*. 8 (2020) e00137.
- [30] M. Čudina, J. Prezelj, I. Polajnar, Use of Audible Sound For On-Line Monitoring of Gas Metal Arc Welding Process, *Metallurgija*. 47 (2008).
- [31] J. Horvat, J. Prezelj, I. Polajnar, M. Čudina, Monitoring Gas Metal Arc Welding Process by Using Audible Sound Signal, *Strojniški Vestnik - Journal of Mechanical Engineering*; Vol 57, No 3 (2011); *Strojniški Vestnik - Journal of Mechanical Engineering*. (2018). <https://doi.org/10.5545/sv-jme.2010.181>.
- [32] F. Tang, Y. Luo, Y. Cai, S. Yang, F. Zhang, Y. Peng, Arc length identification based on arc acoustic signals in GTA-WAAM process, *Int. J. Adv. Manuf. Technol.* 118 (2022) 1553–1563, <https://doi.org/10.1007/s00170-021-08044-9>.
- [33] K. Pal, S. Bhattacharya, S.K. Pal, Investigation on arc sound and metal transfer modes for on-line monitoring in pulsed gas metal arc welding, *J. Mater. Process. Technol.* 210 (2010) 1397–1410, <https://doi.org/10.1016/j.jmatprotec.2010.03.029>.
- [34] K. Pal, S.K. Pal, Monitoring of Weld Penetration Using Arc Acoustics, *Mater. Manuf. Process.* 26 (2011) 684–693, <https://doi.org/10.1080/10426910903496813>.
- [35] Y. Li, J. Polden, Z. Pan, J. Cui, C. Xia, F. He, H. Mu, H. Li, L. Wang, A defect detection system for wire arc additive manufacturing using incremental learning, *Journal of Industrial Information, Integration*. (2021), <https://doi.org/10.1016/j.jii.2021.100291> 100291.
- [36] R. Reisch, T. Hauser, B. Lutz, M. Pantano, T. Kamps, A. Knoll, Distance-Based Multivariate Anomaly Detection in Wire Arc Additive Manufacturing, in: 2020 19th IEEE International Conference on Machine Learning and Applications (ICMLA), 2020: pp. 659–664. <https://doi.org/10.1109/ICMLA51294.2020.00109>.
- [37] I. Polajnar, Z. Bergant, J. Grum, ARC welding process monitoring by audible sound, in: 12th International Conference of the Slovenian Society for Non-Destructive Testing: Application of Contemporary Non-Destructive Testing in Engineering, ICNDT 2013–Conference Proceedings, 2013: pp. 613–620.
- [38] F. Tang, Y. Luo, Y. Cai, S. Yang, F. Zhang, Y. Peng, Arc length identification based on arc acoustic signals in GTA-WAAM process, *Int. J. Adv. Manuf. Technol.* (2021), <https://doi.org/10.1007/s00170-021-08044-9>.
- [39] L. Zhu, Y. Luo, J. Han, C. Zhang, J. Xu, D. Chen, Energy characteristics of droplet transfer in wire-arc additive manufacturing based on the analysis of arc signals, *Measurement* 134 (2019) 804–813, <https://doi.org/10.1016/j.measurement.2018.10.048>.
- [40] J. Xiong, Y.-J. Li, Z.-Q. Yin, H. Chen, Determination of Surface Roughness in Wire and Arc Additive Manufacturing Based on Laser Vision Sensing, *Chinese Journal of Mechanical Engineering*. 31 (2018) 74, <https://doi.org/10.1186/s10033-018-0276-8>.
- [41] T. Hauser, R.T. Reisch, S. Seebauer, A. Parasar, T. Kamps, R. Casati, J. Volpp, A.F. H. Kaplan, Multi-Material Wire Arc Additive Manufacturing of low and high alloyed aluminium alloys with in-situ material analysis, *J. Manuf. Process.* 69 (2021) 378–390, <https://doi.org/10.1016/j.jmapro.2021.08.005>.
- [42] Y. Ma, Z. Hu, Y. Tang, S. Ma, Y. Chu, X. Li, W. Luo, L. Guo, X. Zeng, Y. Lu, Laser opto-ultrasonic dual detection for simultaneous compositional, structural, and stress analyses for wire + arc additive manufacturing, *Addit. Manuf.* 31 (2020), <https://doi.org/10.1016/j.addma.2019.100956> 100956.
- [43] M. Trypuć, K. Białowicz, CaCO<sub>3</sub> production using liquid waste from Solvay method, *J. Clean. Prod.* 19 (2011) 751–756, <https://doi.org/10.1016/j.jclepro.2010.11.009>.
- [44] B. Wu, Y. Li, X. Li, J. Zhu, R. Ma, S. Hu, Organochlorine Compounds with a Low Boiling Point in Desalted Crude Oil: Identification and Conversion, *Energy Fuel* 32 (2018) 6475–6481, <https://doi.org/10.1021/acs.energyfuels.8b00205>.
- [45] J.A. Osunbitan, D.J. Oyedele, K.O. Adekalu, Tillage effects on bulk density, hydraulic conductivity and strength of a loamy sand soil in southwestern Nigeria, *Soil Tillage Res.* 82 (2005) 57–64, <https://doi.org/10.1016/j.still.2004.05.007>.
- [46] M.J. Shensa, The discrete wavelet transform: wedding the a trous and Mallat algorithms, *IEEE Trans. Signal Process.* 40 (1992) 2464–2482.
- [47] I. Daubechies, The wavelet transform, time-frequency localization and signal analysis, Princeton University Press, 2009.
- [48] A.B. and O.N. M. Nibouche, Rapid prototyping of biorthogonal discrete wavelet transforms on FPGAs, IEEE International Conference on Electronics, Circuits and Systems (Cat. No.01EX483). 3 (2001) 1399–1402. <https://doi.org/10.1109/ICECS.2001.957476>.
- [49] Y.S. Wang, Sound quality estimation for nonstationary vehicle noises based on discrete wavelet transform, *J. Sound Vib.* 324 (2009) 1124–1140, <https://doi.org/10.1016/j.jsv.2009.02.034>.
- [50] F. Chung, Chapter 1, Spectral Graph Theory, Eigenvalues and the Laplacian of a graph, 1997, pp. 1–22.
- [51] C.M. Borror, D.C. Montgomery, G.C. Runger, Robustness of the EWMA Control Chart to Non-Normality, *J. Qual. Technol.* 31 (1999) 309–316, <https://doi.org/10.1080/00224065.1999.11979929>.
- [52] J.F. MacGregor, T.J. Harris, [Exponentially Weighted Moving Average Control Schemes: Properties and Enhancements]: Discussion, *Technometrics* 32 (1990) 23–26.
- [53] Z. Li, C. Zou, Z. Gong, Z. Wang, The computation of average run length and average time to signal: an overview, *J. Stat. Comput. Simul.* 84 (2014) 1779–1802, <https://doi.org/10.1080/00949655.2013.766737>.
- [54] X. Zhao, A. Imandoust, M. Khanzadeh, F. Imani, L. Bian, Automated Anomaly Detection of Laser-Based Additive Manufacturing Using Melt Pool Sparse Representation and Unsupervised Learning, In: 2021 International Solid Freeform Fabrication Symposium, University of Texas at Austin, 2021.
- [55] A. Gaikwad, R.J. Williams, H. de Winton, B.D. Bevans, Z. Smoqi, P. Rao, P.A. Hooper, Multi-Phenomena Data Fusion for Enhanced Process Monitoring in Laser Powder Bed Fusion, Available at SSRN 4062535. (n.d.).
- [56] Z. Smoqi, A. Gaikwad, B. Bevans, M.H. Kobir, J. Craig, A. Abul-Haj, A. Peralta, P. Rao, Monitoring and prediction of porosity in laser powder bed fusion using physics-informed meltpool signatures and machine learning, *J. Mater. Process. Technol.* 304 (2022), <https://doi.org/10.1016/j.jmatprotec.2022.117550> 117550.